Photocatalytic oxidation of methane to methanol by tungsten trioxide-supported atomic gold at room temperature

Yi Zeng [a,1], Zhiyuan Tang [b,1], Xingyang Wu [a,1], Anhua Huang [a], Xin Luo [b,*], Guo Qin Xu [c], Yongfa Zhu [d], Song Ling Wang [a,*]

[a] *School of Environmental Science and Engineering, Shanghai Jiao Tong University, 800 Dongchuan Road, Shanghai 200240, China*
[b] *State Key Laboratory of Optoelectronic Materials and Technologies, Guangdong Key Laboratory of Magnetoelectric Physics and Devices, Centre for Physical Mechanics and Biophysics, School of Physics, Sun Yat-sen University, Guangzhou 510275, China*
[c] *Department of Chemistry, National University of Singapore, 117543, Singapore*
[d] *Department of Chemistry, Tsinghua University, Beijing 100084, China*

ARTICLE INFO

ABSTRACT

Atomic-scale metals as active center have been widely investigated for efficient photocatalysis. Understanding the specific electronic structure of atomic-scale center is of profound fundamental importance for superior catalytic performance. Here, we report an atomically dispersed gold on tungsten trioxide (Au_1/WO_3) catalyst for photocatalytic oxidation of methane toward value-added methanol. The Au_1 species reveal a specific tip-enhanced local electrons field which favors the C-H dehydrogenation of methane and thus form methanol (up to 589 $\mu mol\ g^{-1}\ h^{-1}$). Both experimental and theoretical results demonstrate such tip-enhanced effect enhance the catalytic activity of methane oxidation. The theoretical calculations further reveal a lower adsorption energy of product methanol on Au_1, in contrast to Au particles, which suppresses the overoxidation of methanol, and thus promotes its selectivity. Establishing the relationship between electronic density and catalytic activity may create a platform for designing efficient atomic-scale catalysts for C1 catalysis and green chemistry.

1. Introduction

Methane (CH_4), as the principal constituent of natural gas, is widely used as an important fuel and feedstock material in industry [1–3]. However, emission of CH_4 may cause global warming as a result of greenhouse effect, which is around ~23 times higher than that of carbon dioxide (CO_2) [4–7]. Therefore, CH_4 conversion to value-added hydrocarbon chemicals is significant to realize sustainable energy and environment [8–11]. The preferable product of CH_4 conversion is methanol (CH_3OH) which can be directly used as fuel source [12,13]. Given the intrinsic inertness of CH_4 with strong C-H bond (434 kJ mol^{-1}), and negligible electron affinity, harsh reactive conditions of thermal catalysis such as high temperature (> 700 °C) are required to convert CH_4 to CH_3OH, leading to energy consumption and low selectivity of CH_3OH [10,14,] Photocatalysis using solar energy could drive many tough reactions at ambient conditions, such as water splitting and CO_2 reduction. Most recently, photocatalytic methane conversion has attracted increasing interest by using solar energy at room temperature. Typical

semiconductors catalysts, such as TiO_2 and ZnO supported co-catalysts i. e., Ag, have been demonstrated to exhibit good photocatalytic activity in gas-phase CH_4 oxidation [15,16]. In such systems, O_2 is generally activated into active oxygen species, such as $\bullet O_2^-$, ultimately leading to serious over-oxidation of CH_4 into HCHO, CO_2, or CO as the main products [17].

Aqueous-phase photocatalysis enables oxidation of CH_4 to generate more liquid oxygenates, such as CH_3OH. For instance, oxidation of CH_4 to CH_3OH via photocatalysis has been recently reported over FeO_x/TiO_2 with oxidant H_2O_2 [18]. As the crucial point to selectively generate CH_3OH is hydrogen abstraction of CH_4, [19] $\bullet OH$ radical is remarkably responsible for dehydrogenation of CH_4 to form $\bullet CH_3$ radical [20,21]. In nature, the dimeric Fe species as active sites for direct and selective oxidation of CH_4 to CH_3OH by methane monooxygenase enzymes in aqueous condition [22,23]. Furthermore, TiO_2-based Fe species as an efficient catalyst has recently been reported for photocatalytic selective oxidation of CH_4 to CH_3OH in aqueous solution using H_2O_2 as oxidant to generate $\bullet OH$ [18,24]. Thereby, Fe species co-catalyst-H_2O_2 oxidant

---

system plays important roles in determining CH_3OH generation.

Worth noting is that employing co-catalysts is crucial to improve the efficiency of CH_3OH generation, such as noble metals (Au, Ag, Pt, etc.) on semiconductors (i.e., TiO_2, WO_3) [25]. Interestingly, Au is remarkably active for selective hydrocarbon oxidation because of its high electronegativity [26,27]. Notably, dehydrogenation of CH_4 to form methyl ($\bullet CH_3$) radical is favored on Au [28]. Owing to high cost and natural scarcity of Au, however, utilizing Au in cost-effective way remains the major challenging circumstance. Interestingly, atomic scale metals contribute to very distinguished catalytic behavior from their bulk or nanoparticles because of maximized utilization of active sites [29–32]. Furthermore, the cationic character of atomically dispersed metals is expected to have a minimal number of choices of binding sites for reactants or intermediates [29]. Therefore, atomic scale Au potentially exhibits higher reactive activity than their bulk nanoparticles, owing to multiple types of reactive sites [33,34]. On the other hand, atomic scale Au with low coordination number can prohibit the successive dehydrogenation of CH_4, stabilizing the formed $\bullet CH_3$ radical which is a key intermediate for selective generation of CH_4OH. Consequently, manufacturing Au into atomic scale is a promising route to activate CH_4 during the photocatalytic process.

Herein, we applied tungsten trioxides-supported Au atoms (Au_1/WO_3) as catalyst for oxidation of CH_4 with visible light. The Au_1/WO_3 material exhibits specific electronic structure and tip-enhanced local electric field which are favorable for activating CH_4 based on theoretical calculations. Further, the $\bullet OH$ radical formed is crucial to promote the selectivity of methanol product. Based on experimental and theoretical results, radicals-pathway mechanism and four-step reaction routs are suggested to account for the methane oxidation reaction.

2. Experimental

2.1. Synthesis of Au_1/WO_3

The atomic-scale gold on tungsten trioxides (Au_1/WO_3) was prepared by a simple photochemical reduction approach room temperature. Typically, under vigorous stirring, WO_3 (20 mg) and $HAuCl_4 \cdot 3H_2O$ (60 μl, 1.0 mg/mL) aqueous solution were added into deionized water (20 mL) to obtain precursor solution. Such solution was subjected to sonication for – 5 min, followed by UV-light driven photochemical reaction to form atomic-scale Au_1. Notably, 300 W Xenon lamp works as light source. Afterwards, the pink precipitate was finally obtained, after reaction for 20 min under light irradiation. Subsequently, the product denoted as Au_1/WO_3 was collected after washing with deionized water and drying at 60 °C for 12 h in air. With the same experimental process, the content of gold was regulated with different dosage of $HAuCl_4 \cdot 3H_2O$. The as-formed products were denoted as Au_x/WO_3 (x = 0.8, 1, 3, 5 and 8) with Au (0.08, 0.16, 0.30, 0.49, and 0.80 wt%), respectively. The concrete amount of Au in Au_x/WO_3 samples was determined by inductively coupled plasma atomic emission spectroscopy (ICP-AES).

2.2. Synthesis of Au_{Ps}/WO_3

The gold nanoparticles loaded on tungsten trioxides (Au_{Ps}/WO_3) was fabricated via a reduction route. Typically, WO_3 (20 mg) was added into a mixed solution with ethanol (10 mL) and deionized water (10 mL), followed by sonication for 20 min. $HAuCl_4 \cdot 3H_2O$ aqueous solution (1.0 mg/mL, 60 μl) was added to the above solution. Under vigorous stirring, $NaBH_4$ aqueous solution (0.05 M) was dropped into the above solution. Finally, the product (Au_{Ps}/WO_3) was dried at 60 °C for 12 h in air.

2.3. Photocatalytic activity

The photocatalytic reaction for methane conversion to methanol was carried out in an autoclave (130 mL) equipped with a quartz window for light irradiation. A 300 W Xenon lamp as light source is fixed a filter to provide visible light ($\lambda \geq 420$ nm). In a typical experiment, catalyst (20 mg) was dispersed in deionized water (20 mL). Then, both H_2O_2 (200 μl) and $FeCl_2$ aqueous solution (0.01 M, 2 mL) were added to the above solution to get precursor solution. Thereafter, such precursor was transferred to the reaction reactor of photocatalysis, followed by purging methane to remove residue O_2 and air. After that, reactant methane (2.0 MPa) was injected into the reactive reactor. After reaction for 1 h at room temperature (– 25 °C), the reactor containing gas-phase and liquid phases was to be analized after cooling down in an ice bath for 1 h.

2.4. Analysis of products

The products of methane oxidation were analyzed by gas chromatography (GC) and high-performance liquid chromatography (HPLC, SHIMADZU, Essentia CTO-16). The GC equipment was equipped with a thermal conductivity detector (TCD) and two different flame ionization detectors (FID1 and FID2). The gas-phase products was detected by GC, including alkane (CH_4, CH_3CH_3, $CH_3CH_2CH_3$, etc.), gas-phase products (CO, CO_2, H_2, and O_2). Notably, FID1 equipped with high temperature nickel converter for methanizer. We used GC to detect the liquid products, including alcohol (such as CH_3OH, CH_3CH_2OH, $CH_3CH_2CH_2OH$, etc.) and aldehydes (such as CH_3CHO, CH_3CH_2CHO, etc.), and ketones (such as CH_3CH_3CO) by FID2. The liquid organic hydrocarbon acids (e. g., CH_3COOH, HCOOH, etc.) were analyzed on a HPLC (Shodex). Notably, to quantify products accurately, their calibration curves were made in advance.

Additionally, we used a acetylacetone color-developing method to precisely detect HCHO product. Typically, HCHO in the acetic acid-ammonium acetate buffer solution (pH = 6) can react with acetylacetone and ammonia to form yellow-colored 3,5-diacetyl-1,4-dihydrolutidine which presents a characteristic UV–visible absorption at 413 nm. Actually, HCHO aqeous solution has a certain concentration which is proportional to the intensity of absorption at 413 nm.

3. Results and discussion

3.1. Synthesis and characterizations of Au_1/WO_3 catalyst

We synthesized tungsten trioxide-supported atomic gold (Au_1/WO_3) nanoparticles via a photo-reduction approach [2]. Fig. S1 shows monoclinic phase (JCPDS 43-1035) of WO_3 for Au_1/WO_3 material, while the typical signal of Au was not detectable in such XRD patterns. Apart from WO_3 particles, the lattice of Au was absent in the HRTEM image (Fig. S2) of Au_1/WO_3, which is consistent with result of XRD patterns (Fig. S1). As a matter of fact, the signal of Au was detectable in the energy dispersive of spectroscopy (EDS) spectrum of Au_1/WO_3 (Fig. S3). Moreover, the EDS elemental mapping clearly showed the highly uniform dispersion of Au, W, and O elements in Fig. 1(b–d). For comparison, the –1.3 wt% Au nanoparticles/WO_3 (Au_{Ps}/WO_3) material was also synthesized by the $NaBH_4$ chemical reduction route.[2] Au_{Ps}/WO_3 material clearly presents the lattice structure of neutral and bulk Au particles, as displayed by TEM and HRTEM images in Fig. S4.

To directly image the local structure of Au species, we performed abreaction corrected atomic-resolution high angle annular dark-field scanning transmission electron microscope (AC-HAADF-STEM) on the Au_1/WO_3 material. As shown in Fig. 1e, bright contrast spots located on the surface of WO_3 refer to the atomically dispersed Au species in the form of single atoms and atomic clusters circled. Such result perfectly agrees with the analysis of EDS and elemental mapping, further confirming the atomically dispersed Au decorated on the surface of WO_3. Additionally, we performed the extended X-ray-absorption fine-structure (EXAFS) in order to directly investigate the atomic Au species in Au_1/WO_3 material. Despite of the similar atomic numbers Au (Z_{Au} = 79) and W (Z_W = 74) and small amount of Au (– 0.1 wt%), we still achieves partially useful information based on EXAFS spectrum of Au_1/ WO_3 in Fig. S5. In comparison with Au foil, the EXAFS peaks of Au_1/
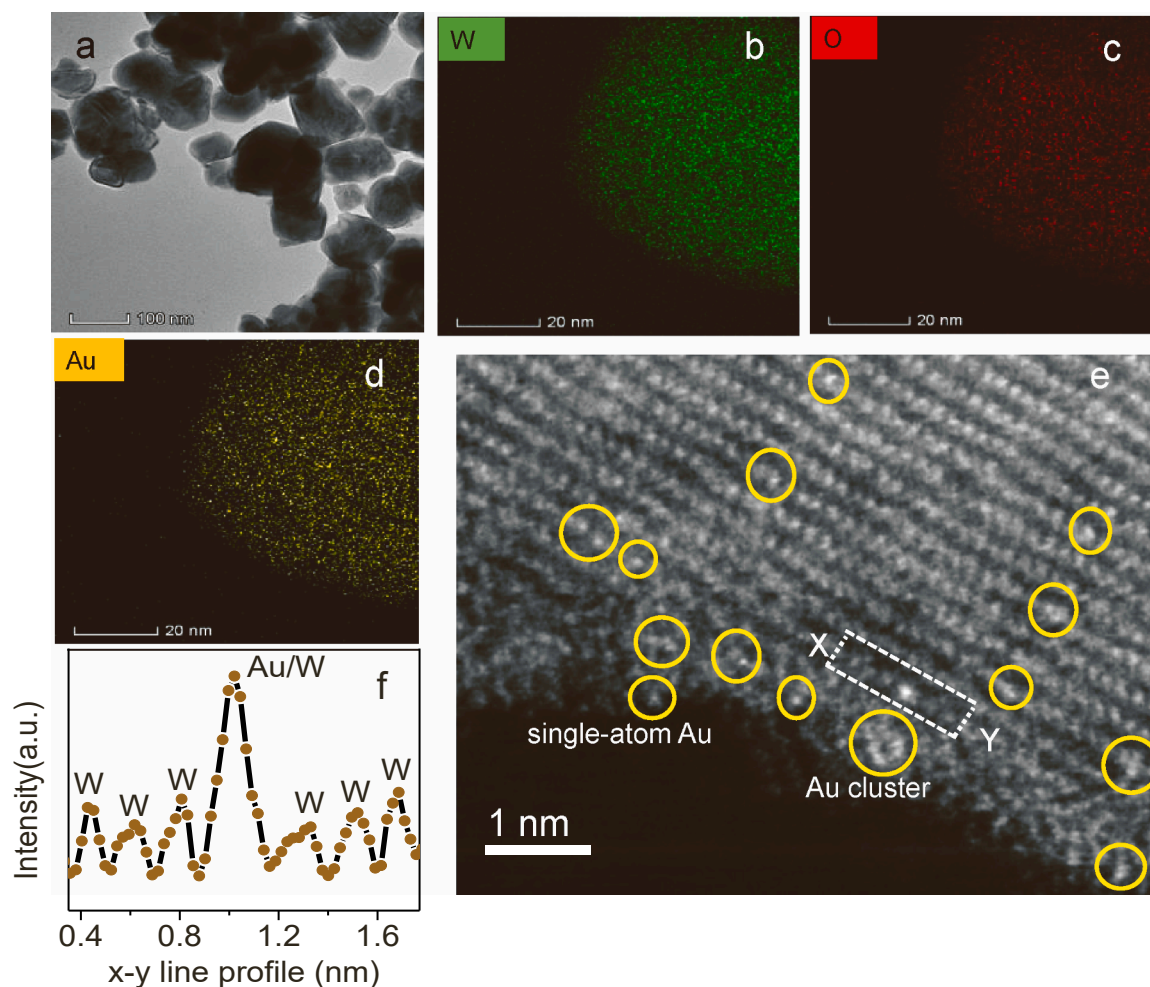
Fig. 1. Characterizations of Au_1/WO_3 material: (a) TEM image; (b–d) Elemental mapping indicating the elements distributions of W, O, and Au. (e) Abreaction corrected atomic-resolution high angle annular dark-field scanning transmission electron microscope (AC-HAADF-STEM) image of Au_1/WO_3 and (f) x–y line scan profile, measured from white-dashed rectangle in e.

WO_3 material at 2.2 Å and 3.0 Å corresponds to the Au-O and Au-Au bonds, respectively. Such case is consistent with the single atoms and clusters of Au tested in AC-HAADF-STEM image (Fig. 1e).

3.2. Theoretical study of electronic structure of Au_1/WO_3 catalyst

Density functional theory (DFT) calculations were performed to study the specific electronic properties of Au_1/WO_3 material (see the structural models in Fig. 2a). As shown in Table S1, the binding energy of Au is -4.635 eV and -0.965 eV for Au_1/WO_3 and Au_{Ps}/WO_3, respectively, indicating a strong interaction between Au_1 and WO_3. Further, more valance electrons concentrate on configuration of Au_1 based on bader charges in Table S1, favoring activation of CH_4 for Au_1/WO_3 catalyst. In Fig. 2d, the projected density of states (PDOS) of Au_1/WO_3 material demonstrates that more electronic states near the Fermi level (E_f), indicating more electrons involved in catalytic process. In contrast, the major bands of Au-5d mainly located from -0.5 eV to -4 eV for Au_{Ps}/WO_3 (Fig. 2e), which shifts the center of d-bands away from the E_f. As a result, the catalysis over Au_{Ps}/WO_3 needs to overcome a larger barrier according to D-bands catalytic theory [35]. And the molecules adsorption will be hampered by the localized electrons due to the stronger Au-Au and Au-WO_3 interaction. Taken together, Au_1/WO_3 presents more electronic states at E_f, which is favoring the catalysis process. In addition, the Au_1 site in Au_1/WO_3 material shows a tip-enhanced effect in Fig. 2c, compared with Au_{Ps} nanoparticles in Au_{Ps}/WO_3 (Fig. 2f), suggesting more electrons to facilitate the activation

of methane molecule.

Based on the AC-HAADF-STEM image of the catalyst and the EXAFS data of Au_1/WO_3 and Au foil materials, we have constructed different configurations of Au atoms adsorbed on the surface of WO_3. Based on our Density functional theory (DFT) calculations, it is found that the hole site is the most favorable adsorption site for the atomic-scale Au species, as shown in Table S2. The strong interaction between Au_1 and WO_3 is also reflected in its large binding energy of -4.635 eV and -0.965 eV for Au_1/WO_3. The average Au-O bond length in Fig. S6 is 1.922Å, which is consistent with the EXAFS results in Fig. S5.

3.3. Photocatalytic activity of methane oxidation

To evaluate the photocatalytic activity of Au_1/WO_3 materials, we first evaluated the selective oxidation of CH_4 towards CH_3OH with visible light. Notably, the WO_3 and Au_{Ps}/WO_3 materials were used for comparison. As shown in Fig. 3a, the as-prepared Au_1/WO_3 catalyst exhibited better performance on generation of CH_3OH in μmol g^{-1} h^{-1}: 589 (Au_1/WO_3, -0.1 wt% Au) > 367 (Au_{Ps}/WO_3, -1.3 wt% Au) > 253 (WO_3). Further, we also evaluated the activity of methane oxidation over Au_x/WO_3 series ($Au_{0.8}/WO_3$, Au_3/WO_3, Au_5/WO_3, and Au_8/WO_3) synthesized via the same method with Au_1/WO_3 material by changing the Au contents. As shown in Fig. S7, these Au/WO_3 series gave rise to a lower generation and selectivity of CH_3OH than that of Au_1/WO_3. In this case, the $Au_{0.8}/WO_3$ catalyst possesses less quality of Au (0. 08 wt%) based on the chemical elemental analysis (plasma atomic emission

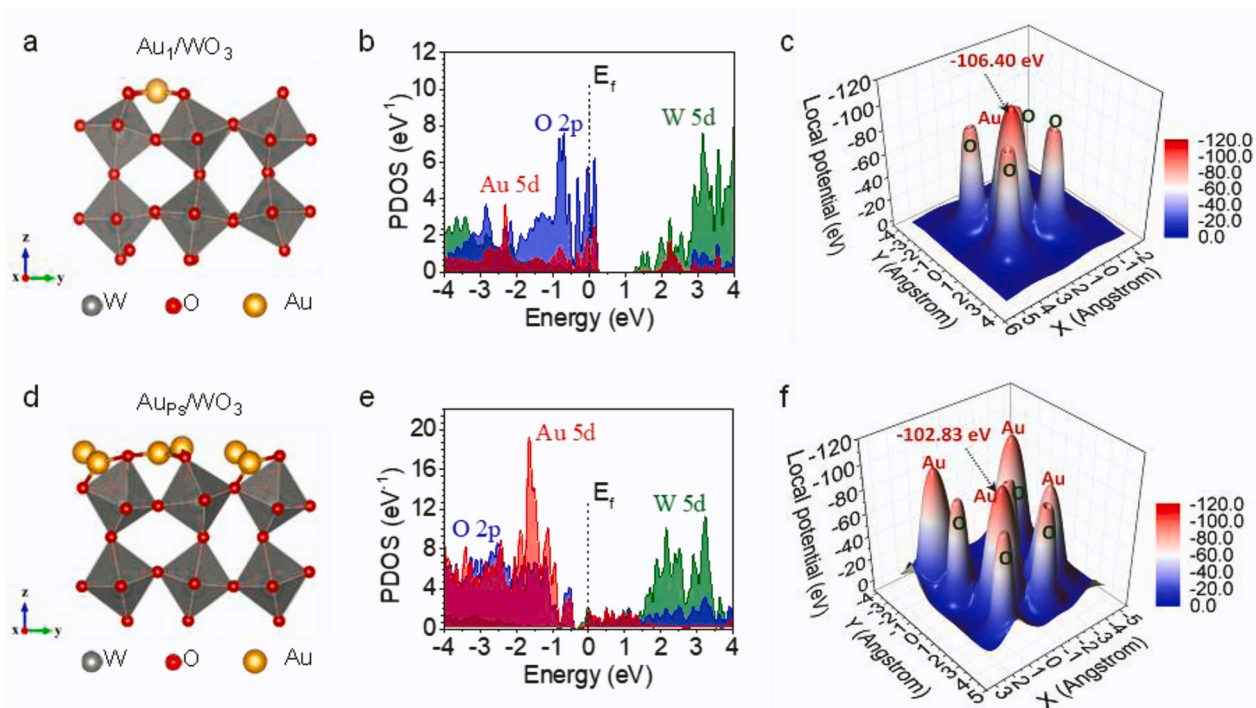**Fig. 2.** DFT theoretical calculations upon the electronic properties of Au_1/WO_3 and Au_{Ps}/WO_3. Schematic atomic structures of (a) Au_1/WO_3 and (d) Au_{Ps}/WO_3 (W: gray, O: red, Au: golden). Projected density of states (PDOS) of (b) Au_1/WO_3 and (e) Au_{Ps}/WO_3. Electronic potentials of Au plane in (c) Au_1/WO_3 and (f) Au_{Ps}/WO_3.

spectroscopy, ICP-AES), suggesting insufficient active sites of Au species for interacting with methane molecule, in comparison with Au_1/WO_3 with 0.1 wt% of Au. On the other hand, although more Au species were formed in the Au_3/WO_3 (Au, 0.3 wt%), Au_5/WO_3 (Au, 0.5 wt%), and Au_8/WO_3 (Au, 0.8 wt%) materials, most of such Au species are in agglomeration, even forming Au nanoparticles (see TEM images in Fig. S8). The aggregated level of Au species shows a significantly intrinsic difference, such as electronic structure based on the calculations result in Fig. 2. Thus, Au_1/WO_3 catalyst presents a higher yield of CH_3OH product, as indicated in Fig. S7. Fig. 3b displays that a yield of – 120 moles of CH_3OH per mole Au active sites in 1 h was obtained by Au_1/WO_3 (– 0.1 wt% Au), higher than –5.6 moles for Au_{Ps}/WO_3 (–1.3 wt% Au). This demonstrates that atomically dispersed Au_1 is favorable for the efficient conversion of CH_4 [36–39]. Notably, even though the Au_{Ps} species possess more electrons to participate in the reaction of CH_4 oxidation, the strong interaction between product CH_3OH and Au_{Ps} will hinder the desorption of the product CH_3OH, leading further overoxidation of CH_3OH. Moreover, a larger overpotential is formed for Au_{Ps}/WO_3. Thus, more over-oxidative by-products, such as HCOOH, were formed for Au_{Ps}/WO_3 catalyst, as displayed in Fig. 3a. It is noted that both Au_{Ps}/WO_3 and Au_1/WO_3 catalysts exhibit over-oxidative by-products of methane oxidation under solar light (AM 1.5 G) irradiation in Fig. S9, including HCHO, CH_3CHO, HCOOH, CO, and CO_2, hence leading to the low selectivity of CH_3OH, only 15% and 18%, respectively. Such over-oxidative reaction of CH_4 is attributable to the presence of superoxide radicals ($\bullet O_2^-$) created from the UV light-induced dissociation of H_2O_2 [18,40]. Furthermore, the control experiments in Fig. S10 indicate the important role of Fe^{2+} in promoting the yield and selectivity of CH_3OH product under visible light ($\lambda \geq 420$ nm) at room temperature. To confirm the resource of O in CH_3OH, we performed the control experiments without using H_2O_2 and WO_3, respectively. Even though the Au_1/WO_3 was used catalyst, no any products were detected in the CH_4 reaction process (see Fig. S10), suggesting H_2O_2 plays important role in CH_3OH generation. On the other hand, in the absence of WO_3, some products CH_3OH, CH_3CHO, etc., are still generated because of the presence of $\bullet OH$ radical produced from

Fenton reaction between Fe^{2+} and H_2O_2. The $\bullet OH$ activate CH_4 to form $\bullet CH_3$, followed by the formation of CH_3OH on a base of reaction ($\bullet OH+$ $\bullet CH_3 \rightarrow CH_3OH$). Taken together, we conclude that the O element of product CH_3OH is from H_2O_2. Additionally, we employed NMR spectroscopy to probe all possible products and intermediate by-products. The typical peaks of CH_3OH and HCHO ($HOCH_2OH$) products were clearly detectable in Fig. 3e and f. Moreover, the peaks associate with intermediate CH_3OOH appeared at 65 ppm in the ^{13}C NMR spectrum (Fig. 3e) and at 3.78 ppm in ^1H NMR spectrum (Fig. 3f). We did not observe the peak of CH_3OOH, however, by high efficiency liquid chromatography, probably due to trace amount and thus be limited to be detected. Additionally, we also made a clear comparison on the photocatalytic methane oxidation of the reported various catalysts-oxidants systems, as shown in Table 1. The comparisons of selectivity and yield of CH_3OH of different single-metals catalysts is shown in Fig. S11. Further, the stability of Au_1/WO_3 catalyst was proved by cycling test, as shown in Fig. S12.

3.4. Role of atomic Au in activating methane

To gain a better understanding of the nature of selective formation of CH_3OH, the active species produced were further assessed by a combined study of electron paramagnetic resonance (EPR) and trapping experiments of active species. It is clear that the Au_1/WO_3 material generates the typically active species, including hydroxyl radical ($\bullet OH$), hydroperoxyl radical ($\bullet OOH$), and methyl radical ($\bullet CH_3$), as displayed in EPR spectra (Fig. 3c). Notably, a slight signal of $\bullet OH$ radical was also observed as a result of the Fenton process in dark ($Fe^{2+} + H_2O_2 \rightarrow Fe^{3+} + \bullet OH$). Furthermore, we performed the trapping experiments to investigate the important roles of these active species in controlling selective generation of CH_3OH in Fig. 3d. Interestingly, e^-, $\bullet OOH$, and $\bullet OH$ species are remarkably determined to the selective formation of CH_3OH. Besides, although h^+ has been trapped, no obvious changes in yield of CH_3OH were found. These trapping experiments, thus, further provide evidences upon the crucial roles of e^-, $\bullet OOH$, and $\bullet OH$ species produced in the Au_1/WO_3 catalyst.
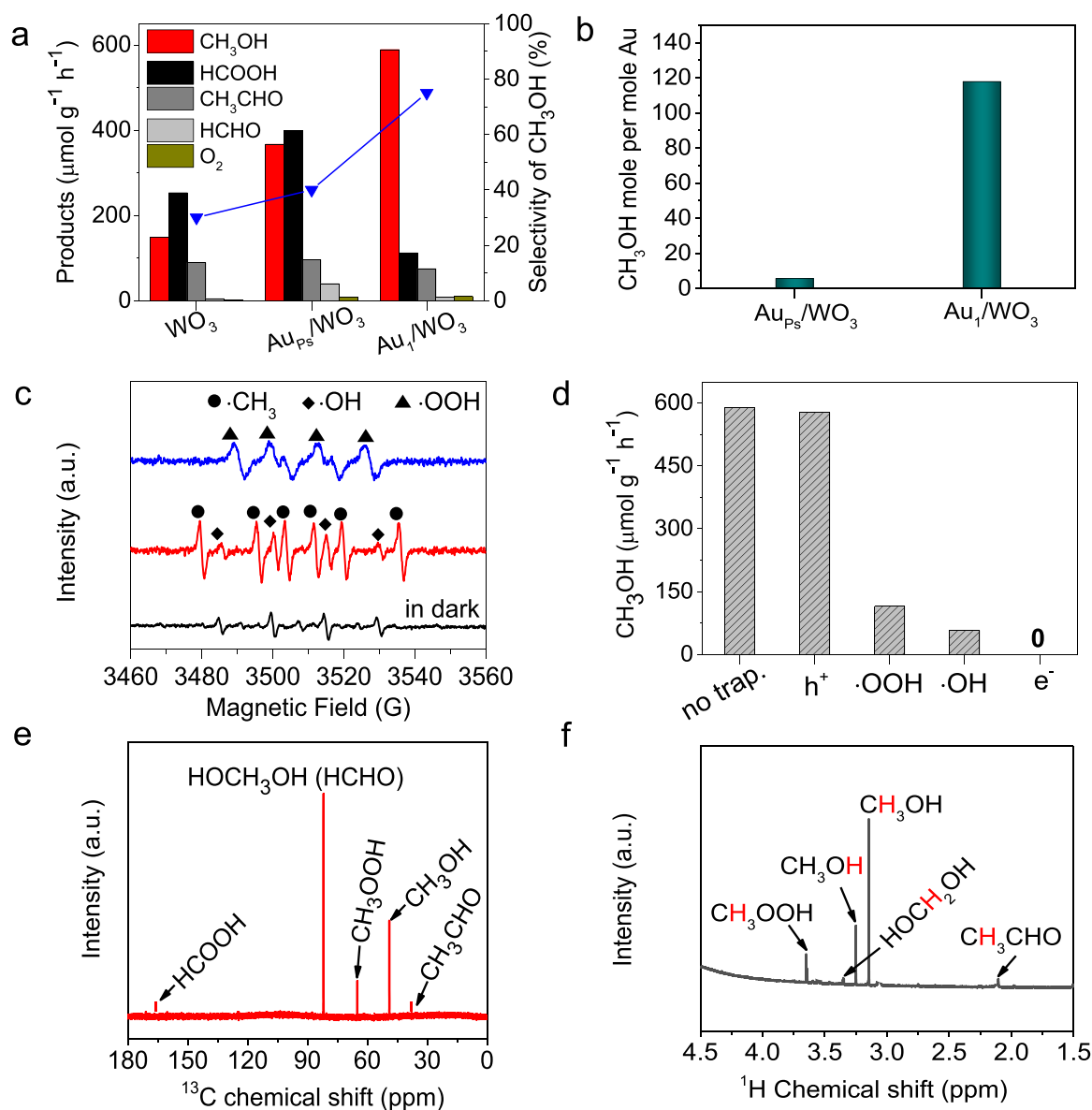
Fig. 3. Photocatalytic activity of CH$_4$ oxidation under visible light ($\lambda \geq 420$ nm) at room temperature (25 °C): (a) Comparison of products and (b) corresponding yields of CH$_3$OH per mole of Au over WO$_3$, Au$_{Ps}$/WO$_3$, and Au$_1$/WO$_3$ catalysts, (c) EPR spectra of •CH$_3$, •OH, and •OOH species detected by using DMPO as trapping reagent after light irradiation for 30 min. Control experiment in dark is used for comparison. (d) Changes in CH$_3$OH after adding scavengers in reaction system for trapping •OOH, e$^-$, h$^+$, and •OH active species, respectively. (e) ^{13}C NMR and (f) ^{1}H NMR spectra of the products from isotope labeling ^{13}CH$_4$ experiment over the Au$_1$/WO$_3$ material.

Table 1
Comparison of various catalysts-oxidants systems for photocatalytic conversion of methane to methanol at room temperature.

Catalysts	Light	Oxidants	Products (µmol g^{-1})					Selectivity of CH$_3$OH (%)	Refs.
			CH$_3$OH	HCHO	C$_2$H$_6$	C$_2$H$_5$OH	CO		
1.2 wt% V-MCM-41	UV ($\lambda > 270$ nm)	NO	10	0	0	0	0	0	[41]
4.8 mol% Au/m-ZnO	300 W Xe lamp (320–2500 nm)	CO$_2$	0	0	40	0	0	0	[42]
6.0 wt% Ag-HPW/TiO$_2$	400 W Xe lamp (UV-Vis)	O$_2$	0	0	0	0	1350	0	[7]
RCN-5	300 W Xe lamp (UV-Vis)	O$_2$	0	0	0	211	0	0	[21]
0.1 wt% Pd/TiO$_2$	300 W Xe lamp (300–500 nm)	O$_2$	0	3410	0	0	0	0	[43]
0.1 wt% Au/TiO$_2$	300 W Xe lamp (300–500 nm)	O$_2$	0	4410	0	0	0	0	[43]
4.8 mol% Au/m-ZnO	300 W Xe lamp (320–2500 nm)	O$_2$	0	0	100	0	0	0	[42]
g-C$_3$N$_4$ @ Cs$_{0.33}$WO$_3$	300 W Xe-lamp (UV-Vis)	O$_2$	9	0	0	0	2	38	[44]
FeN$_x$/C-5–700	1500 W m^{-2} Xe lamp	H$_2$O$_2$	0	0	0	150	0	0	[20]
0.2 wt% Pd$_1$/BP	full arc irradiation (UV)	O$_2$	85	0	0	0	0	72	[36]
0.12 wt% Au/TiO$_2$	full arc irradiation (UV)	H$_2$O$_2$	150	0	0	0	0	30	[45]
0.1 wt% Au$_1$/WO$_3$	300 W Xe lamp ($\lambda > 420$ nm)	H$_2$O$_2$	589	10	0	0	0	75	this work

In addition, the DFT calculations of charge density and PDOS were also performed to study the importance of atomically dispersed Au in controlling selective generation of CH_3OH. It is noted that the adsorbed states of CH_4 and $-CH_3$ on the catalysis are represented by the $*CH_4$ and $*CH_3$, respectively. The charge density plot indicates strong interaction between $*CH_4$ and surface of Au_1/WO_3 catalyst in Fig. 4 [46]. In contrast, strong overlap between $*CH_4$ and O atoms on Au_{Ps}/WO_3 demonstrates the over-binding effect, thus raising the energy barrier for desorption of intermediate products and thus leading to overoxidation, which is consistent with the PDOS in Fig. 4c. Meanwhile, we noted that the bonding and anti-bonding are formed below the E_f when $*CH_3$ adsorbs at Au_{Ps}/WO_3 surface (Fig. 4d). The occupied anti-bonding states will deteriorate the performance of Au_{Ps}/WO_3 for CH_4 conversion as it is energetically instable. In contrast, the anti-bonding states is above the fermi energy (E_f) for Au_1/WO_3 after absorbing $\bullet CH_3$ radical ($*CH_3$), the overall center of the bonding and anti-bonding states is much closer to the Fermi level compared to that of the Au_{Ps}/WO_3. As a result of these changes, the adsorption energy of $*CH_3OH$ on Au_1/WO_3 catalyst is smaller than that on Au_{Ps}/WO_3 (Fig. 4e). This perfectly interprets that Au_1/WO_3 catalyst gave rise to a higher yield and selectivity of CH_3OH product than Au_{Ps}/WO_3. Such case is supported by the fact that Au_1/WO_3 material exhibited stronger photocurrent signal than Au_{Ps}/WO_3, as displayed in Fig. 4f.

3.5. Reaction pathways of methane oxidation

We also calculated reaction path of methane conversion based on the changes of Gibbs energy. The schematic diagram of the catalytic reaction process in Fig. 5a, the H_2O_2 will decompose into two·OH radicals under visible light irradiation. First, the·OH activates $*CH_4$ adsorbed on the Au_1/WO_3 surface to form $*CH_3$ which further reacts with·OH to produce $*CH_3OH$. As revealed by the energy profile in Fig. 5b, the Au_1/WO_3 shows the remarkable downhill tendency of reaction energy towards the final CH_3OH product. Whereas, the $*CH_4$ needs to overcome

an energy barrier of 0.801 eV to transform to the $*CH_3$ for Au_{Ps}/WO_3 catalyst, thus producing less CH_3OH (see Fig. 3b). On the other hand, the adsorption energy of CH_3OH formed on Au_{Ps}/WO_3 catalyst is larger than that of Au_1/WO_3 (Fig. 4e), suggesting that CH_3OH formed on the Au_{Ps}/WO_3 surface is more likely to be further oxidized to by- products, such as HCHO, HCOOH, and CH_3CHO, etc. This perfectly agrees with the experimental result in Fig. 3a on the selectivity of CH_3OH: 75% (Au_1/WO_3) > 41% (Au_{Ps}/WO_3) > 30% (WO_3).

The Gibbs energy profiles on the by-products of the catalysis reaction have also been calculated. As shown in Fig. 5b and S13, the Au_1/WO_3 sample shows the downhill tendency of reaction energy towards the final product CH_3OH, whereas the processes yielding by- products HCHO and HCOOH need to overcome energy barriers (0.176 eV, $*CH_3OOH \rightarrow *HCHO$) and (0.961 eV, $*CH_2 \rightarrow *HCHO$), suppressing over-oxidation reaction of CH_3OH (see Fig. S13 b and d). An energy barrier of 0.801 eV, however, appears in the dehydrogenation process ($*CH_4 \rightarrow *CH_3$) for the Au_{Ps}/WO_3, which does not favor the production of CH_3OH. Furthermore, Au_{Ps}/WO_3 catalyst presents a potential downhill tendency of reaction energy towards the by-products HCHO and HCOOH, leading to over-oxidation of CH_3OH. Notably, the Gibbs energy of $*HCOOH$ is much lower than $*HCHO$ for both Au_1/WO_3 and Au_{Ps}/WO_3 catalysts, so that $*HCHO$ can potentially convert to $*HCOOH$, thus only a few HCHO can be obtained. This is perfectly consistent with the experimental result in Fig. 3a.

To further clearly indicate the involved redox reactions, we summarize involved reactions of methane oxidation. Apart from the Fenton process in dark, activation of CH_4 frequently involves radicals-pathway reactions during the photocatalytic process (Eqs.1–12). In details, the photo-induced charge carriers (e^- and h^+) in Au_1/WO_3 materials (Eq. 1) further undergone the reactive processes of active radicals (Eqs. 2–13). As a matter of fact, the photo-excited e^- can react with H_2O_2 to form $\bullet OH$ radical (Eq. 2). The generated $\bullet OH$ significantly favors the activation of CH_4 to produce methyl ($\bullet CH_3$) radical (Eq. 4). Besides, a part of $\bullet CH_3$ radical could also be generated through the photo-excited h^+ activating

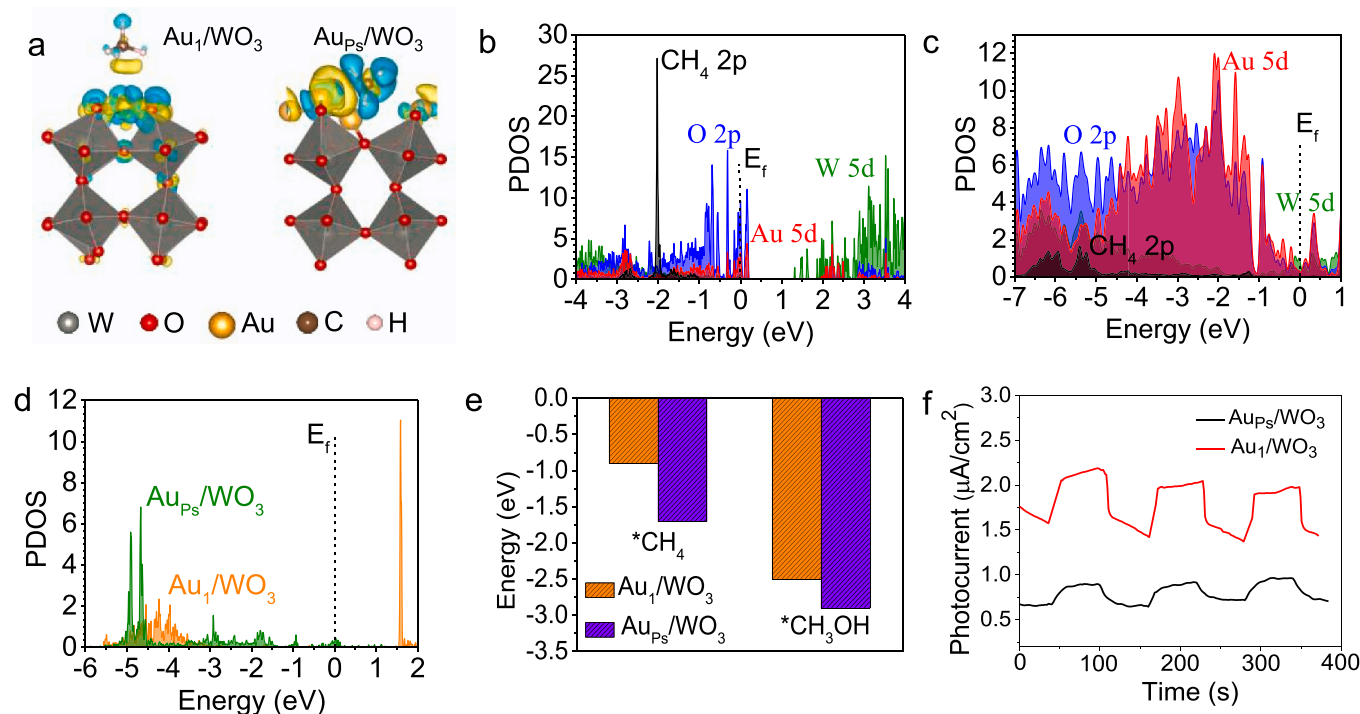**Fig. 4.** DFT calculated electronic properties of CH_4 adsorbed Au_1/WO_3 and Au_{Ps}/WO_3: (a) charge density difference plots with isosurface level of 0.001 e/(Bohr)^3. The yellow and blue areas indicate charge accumulation and charge depletion, respectively. PDOS plot of $*CH_4$ on (b)Au_1/WO_3 and (c)Au_{Ps}/WO_3, respectively. (d) PDOS plot after the $*CH_4$ dehydrogenation to $*CH_3$ on the surface of catalysts. (e) Adsorption energy of CH_4 and CH_3OH on Au_1/WO_3 and Au_{Ps}/WO_3 catalysis. (f) Photocurrent measurement under visible light irradiation.
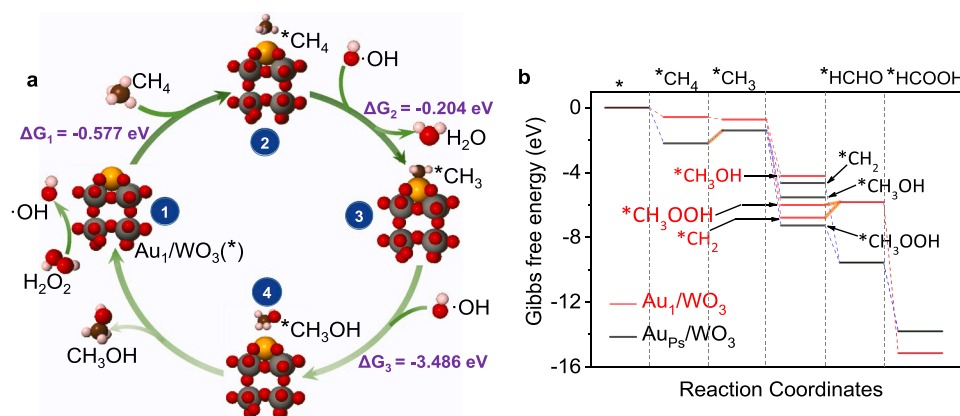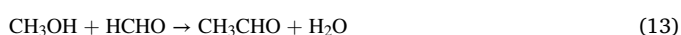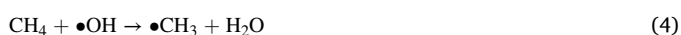
Fig. 5. (a) Schematic diagram of the catalytic reaction process. The red, gray, gold, brown, and pink balls represent O, W, Au, C, and H atoms, respectively. The Gibbs energy differences between the adjacent reaction steps are shown in purple. (b) Reaction energy profile of CH_4 to CH_3OH over Au_1/WO_3 and Au_{Ps}/WO_3.

CH_4 molecule (Eq.5). This is perfectly consistent with the result that large amount of CH_3OH was still detected after trapping h^+ in Fig. 3d. Subsequently, the generated $\bullet CH_3$ enables to react with $\bullet OH$ radical to form CH_3OH (see Eq. 6). On the other hand, $\bullet OOH$ radical was produced as a result of the reaction between $\bullet OH$ and H_2O_2 (Eq. 7), followed by the reaction with $\bullet CH_3$ to form CH_3OOH (Eq. 8). Interestingly, the formed CH_3OOH facilitates the generation of CH_3OH (Eq. 9). In addition to the product CH_3OH, the by-products HCHO ($HOCH_2OH$) and HCOOH were also detectable owning to the over-oxidation of CH_3OH (Eqs. 10–12) [18,47]. Based on experimental result, the generated HCHO enabled to react with CH_3OH to produce the by-product CH_3CHO (Eq.13) [48]. Taken together, $\bullet OH$-based radicals-pathway process enables to promote the closed circle of activation of methane towards CH_3OH.

$$Au_1/WO_3 + h\nu \rightarrow h^+ + e^- \tag{1}$$

$$H_2O_2 + e^- \rightarrow \bullet OH \tag{2}$$

$$H_2O_2 + h^+ \rightarrow O_2 + H^+ \tag{3}$$

$$CH_4 + \bullet OH \rightarrow \bullet CH_3 + H_2O \tag{4}$$

$$CH_4 + h^+ \rightarrow \bullet CH_3 \tag{5}$$

$$\bullet CH_3 + \bullet OH \rightarrow CH_3OH \tag{6}$$

$$H_2O_2 + \bullet OH \rightarrow \bullet OOH + H_2O \tag{7}$$

$$\bullet CH_3 + \bullet OOH \rightarrow CH_3OOH \tag{8}$$

$$CH_3OOH + H^+ + e^- \rightarrow CH_3OH \tag{9}$$

$$CH_3OH + \bullet OH \rightarrow HOCH_2OH \tag{10}$$

$$HOCH_2OH + \bullet OH \rightarrow HCHO + H_2O \tag{11}$$

$$HCHO + \bullet OH \rightarrow HCOOH \tag{12}$$

$$CH_3OH + HCHO \rightarrow CH_3CHO + H_2O \tag{13}$$

4. Conclusions

The atomically dispersed gold decorated on tungsten trioxide (Au_1/WO_3) catalyst exhibits enhanced conversion of methane towards methanol at room temperature under visible light irradiation. The DFT calculations demonstrate that the specific electronic structure of Au_1/WO_3 material. In particular, the tip-enhanced local electronic field at Au_1 sites is further feasible to activate C—H bond of methane. Isotope $^{13}CH_4$ experiment and radical study confirms that the photocatalytic

radical-pathway mechanism is suggested to account for the selective conversion of methane to methanol.

CRediT authorship contribution statement

Yi Zeng: Experiment, Formal analysis, Writing – original draft. **Zhiyuan Tang:** Theoretical calculations, Methodology. **Xingyang Wu:** Experiment, Revision. **Anhua Huang:** Experiment, Investigation. **Xin Luo:** Theoretical calculations, Supervision, Writing – review & editing. **Guo Qin Xu:** Supervision. **Yongfa Zhu:** Supervision. **Song Ling Wang:** Supervision, Writing – review & editing.

Declaration of Competing Interest

The authors declare that they have no known competing financial interests or personal relationships that could have appeared to influence the work reported in this paper.

Appendix A. Supporting information

Supplementary data associated with this article can be found in the online version at doi:10.1016/j.apcatb.2021.120919.

References

[1] J. Ma, X. Tan, Q. Zhang, Y. Wang, J. Zhang, L. Wang, Exploring the size effect of pt nanoparticles on the photocatalytic nonoxidative coupling of methane, ACS Catal. 11 (2021) 3352–3360.

[2] X.Y. Wu, Z. Tang, X. Zhao, X. Luo, S.J. Pennycook, S.L. Wang, Visible-light driven room-temperature coupling of methane to ethane by atomically dispersed Au on WO3, J. Energy Chem. 61 (2021) 195–202.

[3] W. Jiang, J. Low, K. Mao, D. Duan, S. Chen, W. Liu, C.-W. Pao, J. Ma, S. Sang, C. Shu, Pd-modified ZnO–Au enabling alkoxy intermediates formation and dehydrogenation for photocatalytic conversion of methane to ethylene, J. Am. Chem. Soc. 143 (2020) 269–278.

[4] Y. Zeng, X. Luo, F. Li, A. Huang, H. Wu, G.Q. Xu, S.L. Wang, Noble metal-free FeOOH/Li0.1WO3 core–shell nanorods for selective oxidation of methane to methanol with visible–NIR light, Environ. Sci. Technol. 55 (2021) 7711–7720.

[5] T. Kulandaivalu, A.R. Mohamed, K.A. Ali, M. Mohammadi, Photocatalytic carbon dioxide reforming of methane as an alternative approach for solar fuel production-a review, Renew. Sustain. Energy Rev. 134 (2020), 110363.

[6] Z. Shamair, N. Habib, M.A. Gilani, A.L. Khan, Theoretical and experimental investigation of CO_2 separation from CH_4 and N_2 through supported ionic liquid membranes, Appl. Energy 268 (2020), 115016.

[7] X. Yu, V. De Waele, A. Löfberg, V. Ordomsky, A.Y. Khodakov, Selective photocatalytic conversion of methane into carbon monoxide over zinc-heteropolyacid-titania nanocomposites, Nat. Commun. 10 (2019) 1–10.

[8] X. Li, J. Xie, H. Rao, C. Wang, J. Tang, Platinum-and CuOx-decorated TiO_2 photocatalyst for oxidative coupling of methane to C_2 hydrocarbons in a flow reactor, Angew. Chem. Int. Ed. 132 (2020) 19870–19875.

[9] X. Wu, Y. Zeng, H. Liu, J. Zhao, T. Zhang, S.L. Wang, Noble-metal-free dye-sensitized selective oxidation of methane to methanol with green light (550 nm), Nano Res. 1 (2021) 7.

[10] Y. Zeng, H.C. Liu, J.S. Wang, X.Y. Wu, S.L. Wang, Synergistic photocatalysis–Fenton reaction for selective conversion of methane to methanol at room temperature, Catal. Sci. Technol. 10 (2020) 2329–2332.

[11] J. Yang, W. Xiao, X. Chi, X. Lu, S. Hu, Z. Wu, W. Tang, Z. Ren, S. Wang, X. Yu, Solar-driven efficient methane catalytic oxidation over epitaxial $ZnO/La_{0.8}Sr_{0.2}CoO_3$ heterojunctions, Appl. Catal. B: Environ. 265 (2020), 118469.

[12] Y. Tian, L. Piao, X. Chen, Research progress on the photocatalytic activation of methane to methanol, Green Chem. 23 (2021) 3526–3541.

[13] D. Hu, V.V. Ordomsky, A.Y. Khodakov, Major routes in the photocatalytic methane conversion into chemicals and fuels under mild conditions, Appl. Catal. B: Environ. 286 (2021), 119913.

[14] Y. Fan, W. Zhou, X. Qiu, H. Li, Y. Jiang, Z. Sun, D. Han, L. Niu, Z. Tang, Selective photocatalytic oxidation of methane by quantum-sized bismuth vanadate, Nat. Sustain. 4 (2021) 1–7.

[15] X. Yu, V. De Waele, A. Löfberg, V. Ordomsky, A.Y.J.Nc Khodakov, Selective photocatalytic conversion of methane into carbon monoxide over zinc-heteropolyacid-titania nanocomposites, Nat. Commun. 10 (2019) 1–10.

[16] Z. Li, X. Pan, Z.J.Jo.M.C.A. Yi, Photocatalytic oxidation of methane over CuO-decorated ZnO nanocatalysts, J. Mater. Chem. A 7 (2019) 469–475.

[17] H. Song, X. Meng, S. Wang, W. Zhou, X. Wang, T. Kako, J.J.JotA.C.S. Ye, Direct and selective photocatalytic oxidation of CH_4 to oxygenates with O_2 on cocatalysts/ZnO at room temperature in water, J. Am. Chem. Soc. 141 (2019) 20507–20515.

[18] J. Xie, R. Jin, A. Li, Y. Bi, Q. Ruan, Y. Deng, Y. Zhang, S. Yao, G. Sankar, D. Ma, J. Tang, Highly selective oxidation of methane to methanol at ambient conditions by titanium dioxide-supported iron species, Nat. Catal. 1 (2018) 889–896.

[19] C.E. Tinberg, S.J. Lippard, Dioxygen activation in soluble methane monooxygenase, Acc. Chem. Res. 44 (2011) 280–288.

[20] Y. Xing, Z. Yao, W. Li, W. Wu, X. Lu, J. Tian, Z. Li, H. Hu, M. Wu, Fe/Fe_3C boosts H_2O_2 utilization for methane conversion overwhelming O_2 generation, Angew. Chem. Int. Ed. 133 (2021) 8971–8977.

[21] Z. Yang, Q. Zhang, L. Ren, X. Chen, D. Wang, L. Liu, J. Ye, Efficient photocatalytic conversion of CH_4 into ethanol with O_2 over nitrogen vacancy-rich carbon nitride at room temperature, Chem. Commun. 57 (2021) 871–874.

[22] D.Y. Osadchii, A.I. Olivos-Suarez, Á. Szécsényi, G. Li, M.A. Nasalevich, I. A. Dugulan, P.S. Crespo, E.J.M. Hensen, S.L. Veber, M.V. Fedin, G. Sankar, E. A. Pidko, J. Gascon, Isolated Fe sites in metal organic frameworks catalyze the direct conversion of methane to methanol, ACS Catal. 8 (2018) 5542–5548.

[23] S. Sirajuddin, A.C. Rosenzweig, Enzymatic oxidation of methane, Biochemistry 54 (2015) 2283–2294.

[24] H. Song, X. Meng, S. Wang, W. Zhou, S. Song, T. Kako, J. Ye, Selective photo-oxidation of methane to methanol with oxygen over dual-cocatalyst-modified titanium dioxide, ACS Catal. 10 (2020) 14318–14326.

[25] T. Weber, N.A. Wiseman, A. Kock, Global ocean methane emissions dominated by shallow coastal waters, Nat. Commun. 10 (2019) 1–10.

[26] C.J. Wrasman, A. Boubnov, A.R. Riscoe, A.S. Hoffman, S.R. Bare, M. Cargnello, Synthesis of colloidal Pd/Au dilute alloy nanocrystals and their potential for selective catalytic oxidations, J. Am. Chem. Soc. 140 (2018) 12930–12939.

[27] R.D.A.J.C. Durán-Álvarez, D. Ramírez-Ortega, D. Guerrero-Araque, R. Zanella, An alternative method for the synthesis of functional Au/WO_3 materials and their use in the photocatalytic production of hydrogen, Catal. Today 341 (2020) 49–58.

[28] B. László, K. Baán, E. Varga, A. Oszkó, A. Erdőhelyi, Z. Kónya, J. Kiss, Photo-induced reactions in the CO_2-methane system on titanate nanotubes modified with Au and Rh nanoparticles, Appl. Catal. B: Environ. 199 (2016) 473–484.

[29] L. Zhou, J.M.P. Martirez, J. Finzel, C. Zhang, D.F. Swearer, S. Tian, H. Robatjazi, M. Lou, L. Dong, L. Henderson, Light-driven methane dry reforming with single atomic site antenna-reactor plasmonic photocatalysts, Nat. Energy 5 (2020) 61–70.

[30] L. Kuai, Z. Chen, S. Liu, E. Kan, N. Yu, Y. Ren, C. Fang, X. Li, Y. Li, B. Geng, Titania supported synergistic palladium single atoms and nanoparticles for room temperature ketone and aldehydes hydrogenation, Nat. Commun. 11 (2020) 1–9.

[31] A. Wang, J. Li, T. Zhang, Heterogeneous single-atom catalysis, Nat. Rev. Chem. 2 (2018) 65–81.

[32] X.-F. Yang, A. Wang, B. Qiao, J. Li, J. Liu, T. Zhang, Single-atom catalysts: a new frontier in heterogeneous catalysis, Acc. Chem. Res. 46 (2013) 1740–1748.

[33] X. Zhang, Z. Sun, B. Wang, Y. Tang, L. Nguyen, Y. Li, F.F. Tao, C-C coupling on single-atom-based heterogeneous catalyst, J. Am. Chem. Soc. 140 (2018) 954–962.

[34] J.C. Durán-Álvarez, R. Del Angel, D. Ramírez-Ortega, D. Guerrero-Araque, R. Zanella, An alternative method for the synthesis of functional Au/WO_3 materials and their use in the photocatalytic production of hydrogen, Catal. Today 341 (2020) 49–58.

[35] B. Hammer, J.K. Norskov, Why gold is the noblest of all the metals, Nature 376 (1995) 238–240.

[36] L. Luo, J. Luo, H. Li, F. Ren, Y. Zhang, A. Liu, W.-X. Li, J. Zeng, Water enables mild oxidation of methane to methanol on gold single-atom catalysts, Nat. Commun. 12 (2021) 1–10.

[37] N. Agarwal, S.J. Freakley, R.U. McVicker, S.M. Althahban, N. Dimitratos, Q. He, D. J. Morgan, R.L. Jenkins, D.J. Willock, S.H. Taylor, Aqueous Au-Pd colloids catalyze selective CH_4 oxidation to CH_3OH with O_2 under mild conditions, Science 358 (2017) 223–227.

[38] M. Zhong, Y. Xu, J. Li, Z.-X. Ge, C. Jia, Y. Chen, P. Deng, X. Tian, Engineering PdAu nanowires for highly efficient direct methane conversion to methanol under mild conditions, J. Phys. Chem. C 125 (2021) 12713–12720.

[39] B. László, K. Baán, E. Varga, A. Oszkó, A. Erdőhelyi, Z. Kónya, J. Kiss, Photo-induced reactions in the CO_2-methane system on titanate nanotubes modified with Au and Rh nanoparticles, Appl. Catal. B: Environ. 199 (2016) 473–484.

[40] X. Li, C. Chen, J.J.L. Zhao, Mechanism of photodecomposition of $H2O2$ on $TiO2$ surfaces under visible light irradiation, Langmuir 17 (2001) 4118–4122.

[41] Y. Hu, Y. Nagai, D. Rahmawaty, C. Wei, M. Anpo, Characteristics of the photocatalytic oxidation of methane into methanol on V-containing MCM-41 catalysts, Catal. Lett. 124 (2008) 80.

[42] L. Meng, Z. Chen, Z. Ma, S. He, Y. Hou, H.-H. Li, R. Yuan, X.-H. Huang, X. Wang, X. Wang, Gold plasmon-induced photocatalytic dehydrogenative coupling of methane to ethane on polar oxide surfaces, Energy Environ. Sci. 11 (2018) 294–298.

[43] H. Song, X. Meng, S. Wang, W. Zhou, X. Wang, T. Kako, J. Ye, Direct and selective photocatalytic oxidation of CH_4 to oxygenates with O_2 on cocatalysts/ZnO at room temperature in water, J. Am. Chem. Soc. 141 (2019) 20507–20515.

[44] Y. Li, J. Li, G. Zhang, K. Wang, X. Wu, Selective photocatalytic oxidation of low concentration methane over graphitic carbon nitride-decorated tungsten bronze cesium, ACS Sustain. Chem. Eng. 7 (2019) 4382–4389.

[45] J. Xie, R. Jin, A. Li, Y. Bi, Q. Ruan, Y. Deng, Y. Zhang, S. Yao, G. Sankar, D. Ma, Highly selective oxidation of methane to methanol at ambient conditions by titanium dioxide-supported iron species, Nat. Catal. 1 (2018) 889–896.

[46] S. Zhang, Q. Wang, Y. Kawazoe, P. Jena, Three-dimensional metallic boron nitride, J. Am. Chem. Soc. 135 (2013) 18216–18221.

[47] X. Geng, W. Li, F. Xiao, D. Wang, L. Yang, Effect of in situ Fe(ii)/Fe(iii)-doping on the visible light-Fenton-like catalytic activity of Bi/BiOBr hierarchical microspheres, Catal. Sci. Technol. 7 (2017) 658–667.

[48] I. Bar-Nahum, A.M. Khenkin, R. Neumann, Mild, aqueous, aerobic, catalytic oxidation of methane to methanol and acetaldehyde catalyzed by a supported bipyrimidinylplatinum-polyoxometalate hybrid compound, J. Am. Chem. Soc. 126 (2004) 10236–10237.